

RSC Advances



This is an *Accepted Manuscript*, which has been through the Royal Society of Chemistry peer review process and has been accepted for publication.

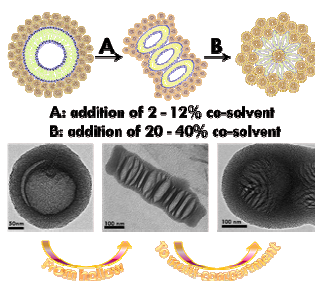
Accepted Manuscripts are published online shortly after acceptance, before technical editing, formatting and proof reading. Using this free service, authors can make their results available to the community, in citable form, before we publish the edited article. This *Accepted Manuscript* will be replaced by the edited, formatted and paginated article as soon as this is available.

You can find more information about *Accepted Manuscripts* in the [Information for Authors](#).

Please note that technical editing may introduce minor changes to the text and/or graphics, which may alter content. The journal's standard [Terms & Conditions](#) and the [Ethical guidelines](#) still apply. In no event shall the Royal Society of Chemistry be held responsible for any errors or omissions in this *Accepted Manuscript* or any consequences arising from the use of any information it contains.

C. X. (Cynthia) Lin, S. Jambhrunkar, P. Yuan,
C. H. Zhou and X. S. Zhao*

RSC Advances, 2015



Multi-compartment periodic mesoporous organosilica materials (MCPMOs) with excellent drug loading and release performance for potential future application in theranostic field.



Journal Name

ARTICLE

Design and synthesis of periodic mesoporous organosilica materials with a multi-compartment structure

C. X. Cynthia Lin,^a S. Jambhrunkar,^a P. Yuan,^b C. H. Zhou^c and X. S. Zhao^{d,*}Received 00th January 20xx,
Accepted 00th January 20xx

DOI: 10.1039/x0xx00000x

www.rsc.org/

Abstract: Recently many scientists are attracted to replicate the unique structure and function of multi-compartment found in natural cells. Despite the success in recreating multi-compartment structure for organic materials, it is a great challenge to translate the similar concept into inorganic and hybrid materials for more versatile applications. Here as the first example in organosilica family, we present a facile synthesis route to create hybrid materials with multi-compartment structure through a spontaneous assembly of fluorocarbon (FC) and hydrocarbon (HC) surfactants with the addition of co-solvent. The formation of multi-compartment periodic mesoporous organosilica (MCPMO) is triggered by the presence of organic co-solvent that induces the osmotic pressure difference in the system. The MCPMO demonstrate a high loading capacity of antimalarial and anticancer drug Artemisinin (47%) with a sustainable release profile contributed by a unique compartmentalized structure and hydrophobic properties. This synthesis strategy can be extended to design various materials with different compositions and morphologies for wider applications including microelectronics, biomedical, catalysis and energy storage.

Introduction

Recent progress in material synthesis has brought new fascinating features to create nanomaterials with more complex domain and morphologies (i.e. Janus, multi-compartment and patchy particles), which is beneficial for diverse potential applications.¹ In particular, nanomaterials with multi-compartment structure are very attractive candidate for drug delivery systems, because they can sequester different compounds within single carrier mimicking eukaryotic cells.^{2,3} Generally multi-compartment materials are made from amphiphilic block copolymer micelles (e.g. ABC mikto arm stars,⁴ BAC triblock copolymers,⁵ diblock copolymers⁶); multiple lipid bilayer or vesosomes,⁷ and electro-hydrodynamic co-jetting process.^{8,9} However, these organic based materials possess shortcomings that may limit their practical applications in a wider range (i.e. leaching problems, thermally and chemically unstable, high production cost, toxicity, premature release of active ingredients).^{10,11} On the other hand, inorganic materials like mesoporous silica nanoparticles (MSNs) offer better stability

compare to liposome and polymeric materials and have been approved by US Food and Drug Administration for stage I clinical trial.¹² However MSNs have hydrophilic characteristic, which may hinder their optimum interaction with many hydrophobic molecules; nevertheless this problem can be overcome by the creation of organosilica materials as their counterpart.

Since the discovery of Periodic mesoporous organosilicas (PMOs) in 1999,¹³⁻¹⁵ these hybrid organic-inorganic materials have attracted many attentions due to their unique feature that allows easy surface modification for multipurpose applications.¹⁶ Unlike MSNs with their hydrophilic nature, these PMOs have hydrophobic characteristic across their framework, which make them as a highly promising platform for catalysis,¹⁷ trafficking drugs, enzymes with higher adsorption capacity,^{18,19} and possess excellent stability in physiological environment.^{20,21} So far PMOs with conventional morphologies of porous spheres, core-shell and rod-like particles have been reported,^{22,23} yet those with higher degree of architectural complexity is less studied. There is a great challenge to tailor hybrid PMOs into multifunctional materials with sophisticated structure and morphology that can potentially fulfil a high demand of emerging industrial applications.²⁴ Moreover, it is necessary to understand the fundamental aspects that govern the formation of PMOs with more complex structure to provide new strategies in controlling the final morphology down to nanometre scale.

Here we introduce a simple approach to fabricate PMOs with unique multi-compartment structure and tunable vesicle size, offering hybrid framework for better interaction with many hydrophobic guest molecules. Our synthesis strategy follows a similar rationale of amphiphilic system, where multi-compartment micelles are formed through the self-assembly of block copolymer micelles as a result of energetic repulsions between different blocks.²⁵ The driving forces for the formation of these segregated

^a Australian Institute for Bioengineering and Nanotechnology, The University of Queensland, Brisbane, QLD 4072, Australia

^b State Key Laboratory of Heavy Oil Processing, China University of Petroleum, Beijing 102249, China.

^c College of Chemical Engineering, Zhejiang University of Technology, Hangzhou, Zhejiang 310014, China

^d School of Chemical Engineering, The University of Queensland, St. Lucia, Brisbane, QLD 4072, Australia

† Electronic Supplementary Information (ESI) available: TEM, SEM, XRD, Nitrogen sorption and pore size distribution of sample M, P and A series; Low magnification TEM image of MCPMO sample; Pore size distribution of E series sample; Tabulated physicochemical properties of MCPMOs from E, M, P, and A series; Tabulated results of drug loading amount. Three dimensional electron tomography movie clips of MCPMOs tilted along x-axis, y-axis, reconstruction of internal area and selected parts of MCPMO individual compartments. See DOI: 10.1039/x0xx00000x

domains lie on the mutual incompatibility between different blocks especially fluorinated (fluorocarbon) and non-fluorinated ones (hydrocarbon).^{26,27} These fluorocarbon blocks commonly undergo phase segregation with a strong tendency to self-aggregate forming vesicles or tubules rather than micelles due to their inherent characteristics of highly surface active, rigid and stable.^{28,29} It is believed that fluorocarbon vesicles have similar characteristics as phospholipid or polymeric vesicles, which are permeable and may undergo adhesion, budding, fission, fusion, multi-compartmentalization, morphology transitions and wetting upon small changes in their environment.³⁰

In this study, we utilize the mutual incompatibility between hydrocarbon (HC) and fluorocarbon (FC) surfactants to form mesoporous shell through liquid crystal template (LCT) and hollow core through vesicle template (VT) mechanism.³¹ This process is followed by the addition of organic co-solvents that play a significant role in the formation of multi-compartment structure of MCPMOs through the changing of osmotic condition in the system. We further observe the effect of different co-solvents including short chain alcohols and non-alcohol for their role to induce morphology transition from singular to multi-vesicular structure. We also studied the potential application of MCPMOs as anticancer drug carrier through their adsorption and release kinetic behavior. Our initial results suggest that MCPMOs with high surface area (>1000 m²/g) and pore volume (>1 cm³/g) show a promising feature as drug carrier with relatively high adsorption capacity (~47%) and sustainable release rate (~46% in 120 hours).

Experimental Section

Chemicals

Hydrocarbon (HC) surfactant (cetyltrimethylammonium bromide, CTAB > 99%) was purchased from Sigma–Aldrich, Fluorocarbon (FC) surfactant FC-4 (C₃F₇O(CFCF₃CF₂O)₂CFCF₃CONH(CH₂)₃N⁺(C₂H₅)₂CH₃I) was purchased from Yick Vic Chemicals (Hong Kong, and sodium hydroxide (NaOH > 97%) was from Merck. Organosilica precursor 1,2-bis(trimethoxysilyl) ethane (BTME 96%) and Artemisinin (ART) were purchased from Sigma–Aldrich. All these chemicals were used without further purification.

Preparation of MCPMO materials

In a typical synthesis, 0.4 g of FC-4 was dissolved in 96 mL of deionized water under stirring at room temperature for 1 h, followed by the addition of 0.25 g of CTAB and 0.7 mL of 2 M NaOH. Afterwards the temperature was increased to 80 °C, at which 0.756 mL of organosilica source was added drop wise under vigorous stirring for 2 h. The white precipitates were collected and filtered, then washed with deionized water and ethanol for five times at room temperature, followed by drying at 70°C to obtain as-synthesized material. To investigate the influence of co-solvents on the morphology and structure of the MCPMO samples, organic co-solvents of ethanol (E), or methanol (M), or propanol (P), or acetone (A) was added into the above mixture with varied concentration. Total amount of solvent (co-solvent and H₂O) was kept constant at 96 ml where the concentration of co-solvent was varied (x)= 0, 1, 2, 3, 6, 8, 12, 20, and 40% (V/V). The molar ratio of reactant is 1 CTAB: 0.64 FC-4: 4.4 organosilica: 7774 H₂O: x ethanol:

2 NaOH. For the addition of ethanol, the samples are denoted as 0E, 1E, 2E, 3E, 6E, 8E, 12E, 20E, and 40E. For the addition of methanol, the samples are denoted as 3M, 6M, and 20M. For the addition of propanol, the samples are denoted as 3P, 6P, and 20P. For the addition of acetone, the samples are denoted as 3A, 6A, and 20A. For template removal, 1.0 g of the as-synthesized sample was added to a mixture of 100 ml of ethanol and 5 ml (HCl 37%), stirred at 60 °C for 24 h. The solid were collected by centrifuge and dried at 70 °C.

Characterization

Powder X-ray diffraction (XRD) pattern were recorded on a Rigaku X-Ray diffractometer, with Co-K α radiation at a scanning rate of 0.5/min and step size of 0.02°. Scanning electron microscopy (SEM) characterization was done using a JEOL JSM-7001F operated at 3-5 kV. Transmission electron microscopy (TEM) characterization was performed on a JEOL JEM-2100 operated at 200kV. Cryo – TEM analysis was carried out using a Philips Technai T12 operated at 120 kV using a 4k FEI Eagle CCD Camera with Serial EM software. Samples were vitrified on C-flat holey carbon grids by FEI Vitrobot Mark 3 (FEI Company, Eindhoven, Netherlands). Three-dimensional electron tomography (3D-ET) analysis was performed through a FEI Tecnai F30 electron microscope operated at 300 kV. All TEM images were recorded at a preset defocus in a bright-field mode to show the sample thickness contrast. The ET specimens were prepared by dispersing the powder samples into ethanol placed in a vial and ultrasonicated for 5 mins, then directly deposited onto copper grids with Formvar supporting films (Proscitech). Colloidal gold particles (10 nm) were deposited on both surfaces of the grids as fiducial/reference markers for the subsequent image alignment procedures. The tomographic tilt series were carried out by tilting the specimen around a single axis under the electron beam. All TEM images were recorded over a tilt range of +60 to -60° with the increments of 1°. Data processing was done through IMOD software. The nitrogen sorption isotherms were measured at -196°C using a Micromeritics Tristar II 3020 system. Samples were degassed at 150°C overnight before adsorption. Specific surface area was calculated by the Brunauer–Emmett–Teller (BET) method using relative pressure (P/P₀) data between 0.05 and 0.3. Pore volume was obtained from the N₂ volume adsorbed at the highest P/P₀ (~0.99). Pore size distribution curves were calculated from the adsorption branch with the Barrett–Joyner–Halenda (BJH) model. UV-visible absorption spectra were recorded using a Shimadzu UV-1700 spectrophotometer.

Drug loading and release

Artemisinin (ART) as anti-tumour model drug was dissolved in ethanol at 2 mg/ml concentration, and 0.1 g of MCPMO samples were added into 5 ml of this solution, followed by shaking the mixture with rotary shaker for 72 h at room temperature. The concentration of ART loaded into the samples were analysed by UV through transforming ART into a UV-absorbing compound with alkaline treatment. The alkali reaction was carried out by adding 1 mL of 0.2M NaOH solution to each sample and heated the mixture at 40 °C for 5 mins then the absorbance was measured by UV spectrophotometer at λ max 290 nm. In-vitro drug release studies were carried out in Phosphate buffer solution (PBS, pH = 4.4). The

initial concentration of ART loaded MCPMO samples were kept consistent at 1 mg. Pristine ART (1 mg) was also prepared as the reference, and each sample was placed into 10 ml of PBS, at 37°C. The released concentration as a function of time was analyzed by UV-Vis spectrophotometer with λ max of 266 nm.

Results and Discussions

Synthesis of multi-compartment periodic mesoporous organosilicas (MCPMOs).

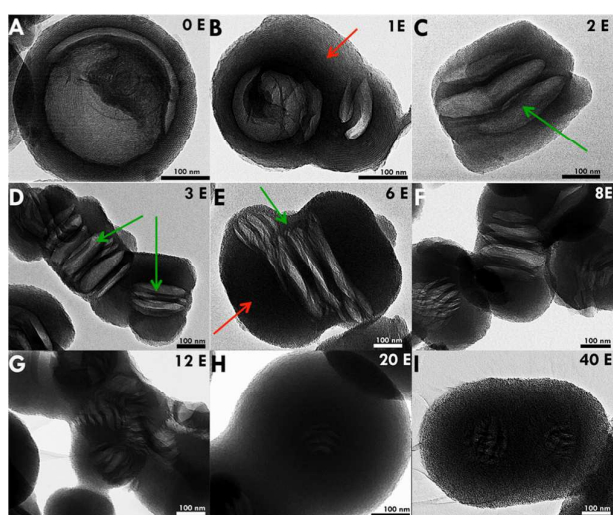


Figure 1. TEM images of MCPMO samples A) 0E, B) 1E, C) 2E, D) 3E, E) 6E, F) 8E, G) 12E, H) 20E, and I) 40E with red arrows point to mesoporous shell areas and green arrows point to the multi-compartment vesicles

MCPMO samples were prepared through dual template mechanism with the addition of different concentration of ethanol (E). The gradual changes of their morphology from a singular to multi-vesicular structure were observed by TEM analysis (Figure 1). Without addition of E, sample 0E showed a core-shell structure with a highly ordered mesoporous shell and a singular hollow core of 250-300 nm size (Figure 1A). However, with the addition of a low concentration E (1-6%), the singular core-shell structure underwent gradual changes and became multi-compartment structure (Figure 1B-E). When (8-12%) E was added, the multi-compartment started to show an irregular curvature (Figures 1F-G), indicating a higher degree of elasticity in their vesicular chains affected by a higher concentration of E. When (20-40%) E was applied, those vesicles were hardly visible due to their tiny size (< 10-20 nm x 90-100 nm) that formed interlaced structure and covered by thick layer of mesoporous shells (Figures 1H-I). Detailed physical properties of these samples were presented in Table 1. TEM images (Figures 1A – I) also revealed that the reduction of vesicle sizes from 300 nm to <10 nm with shape transformation from spherical into oblate or prolate spheroid, followed by interlaced vesicles were mainly attributed to the interaction of FC and the increasing E in the system. In aqueous medium, the immiscible mixture of HC and FC formed opaque solution when stirred below their de-mixing

temperature ($T_d = 51-53$ °C) and formed 2 phases as the stirring ceased.²⁸

However with the addition of 20% E, this opaque solution spontaneously turned into translucent and became transparent when E was >40 %; indicating that the mixture of HC and FC already reached their thermodynamic stability. To investigate the role of co-solvent in the formation of MCPMO, we used methanol (M), propanol (P) and acetone (A) to replace ethanol (E) with 3 concentrations (3, 6, and 20 %). These samples were denoted as 3M/6M/20M, 3P/6P/20P, 3A/6A/20A. The TEM results showed that M, P and A brought similar effect as E to the MCPMOs (supplementary information – Fig.S1), and their detailed physical properties presented in Table S1. Major difference might come from the addition of 3% co-solvents, where 3M showed multi compartment with spherical vesicles but 3E, 3P and 3A showed oblate-prolate vesicles. This suggested that co-solvent with longer carbon chain bring more elasticity towards FC vesicles.

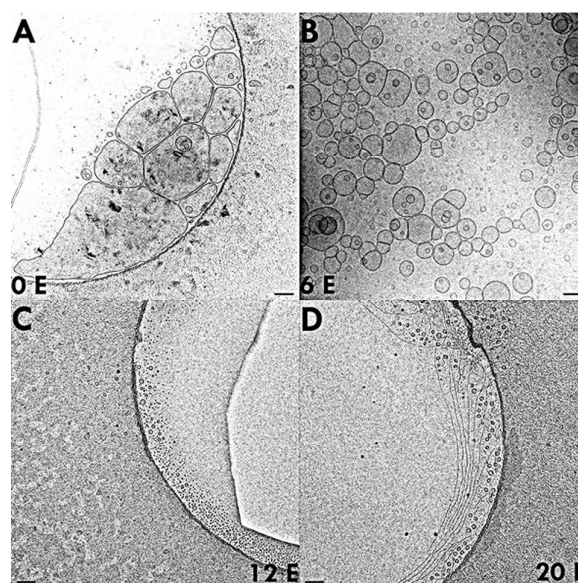


Figure 2. Cryo TEM images of MCPMO samples of A) 0E, B) 6E, C) 12E and D) 20E (Scale bar indicate 100 nm)

Cryo TEM analysis was performed to investigate the internal morphology changes of MCPMOs before condensation process of organosilane. We prepared mixture of FC and HC surfactants in aqueous solution with (0, 6, 12, and 20%) of E. Figure 2 showed a gradual decrease of vesicle sizes from ~ 300-400 nm (0E) to 100-200 nm (6E), then reduced to < 10-20 nm (12E) and finally to ~ 10-25 nm vesicles co-existed with threadlike micelles (20 E). These threadlike micelles might originate from the deflated vesicles that fused together forming long chain. It is noted that the decrease of vesicle size could be triggered by the reduction of vesicles internal content in response to the osmotic changes brought by E. In addition, these vesicles appeared as spherical instead of prolate or oblate spheroids as shown by TEM (Figure 1). This suggested that the transition from spherical vesicles into oblate or prolate spheroids took place during the condensation of organosilica species when FC vesicles and HC micelles had already self-assembled before this stage.

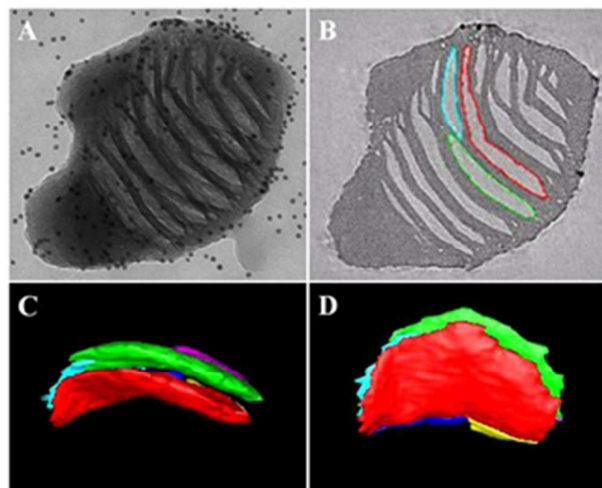


Figure 3. Electron Tomography (ET) of (A) MCPMO sample, (B) thin tomogram slice of A, (C and D) 3D model viewed from different angles of some compartments shown in B.

This unusual phenomenon was further investigated through three dimensional electron tomography (3D-ET) analyses on the chosen sample of 2E, which possessed thin porous shell (Figure 3A - high magnification and Figure S2 - low magnification). The sample was tilted along x-axis (SI-movie clip 1) and y-axis (SI-movie clip 2), showing it contained an array of ellipsoidal vesicles (diameter of ~45-50 nm and length of ~250-280 nm) encapsulated within mesoporous shell. A thin tomogram slice of the sample showed the internal structure of MCPMO as depicted by Figure 3B and SI-movie clip 3), where the vesicles forming isolated compartments and separated by a thin layer of membrane which mimics the eukaryotic cells. A selected area in the isolated compartment of MCPMO sample was further traced to generate a 3D model reconstruction (SI-movie clip 4) as shown by different colour contours and observed from different angles (Figure 3C and D). These isolated compartments were completely independent oblate spheroids, which were likely formed during condensation reaction through a compression of several flexible spherical vesicles into an array of oblate vesicles encased by mesoporous shell.

The external morphology of MCPMO samples was observed through SEM analysis shown by Figure 4. Without the addition of E, the particles were spherical with average size of 300 - 350 nm (Figure 4A and Table 1). With low concentration of E (1-2%), some particles showed single partition lines as highlighted by red arrows and circles (Figures 4B-C). With moderate concentration of E (3-6%), those double and triple partition lines became more noticeable as shown by the red circles and arrows (Figures 4D-E), which was consistent with their corresponding TEM images (Figures 1B-E). For higher concentration of E (8-12%), the partition lines could not be easily identified and the particles started to fuse forming larger size of ~ 350 -750 nm (Figures 4F-G). In particular, sample 12E (Figure 4G) revealed the exposed area of its multi-compartment structure (green circles and arrows), which closely resembled the internal morphology shown by the TEM image Figure 1G. For the addition of

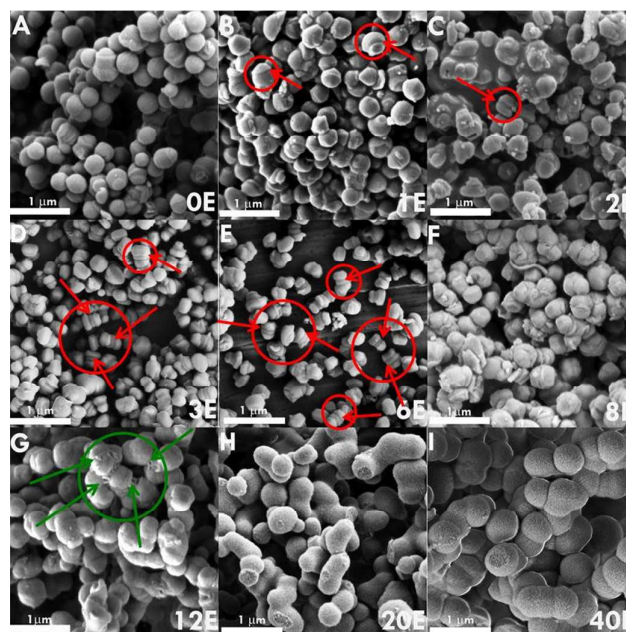


Figure 4. SEM images of MCPMO sample A) 0E, B) 1E, C) 2E, D) 3E, E) 6E, F) 8E, G) 12E, H) 20E, and I) 40E. Red circles and arrows show the partition lines of samples 1E, 2E, 3E and 6E. Green circle and arrows indicate the exposed area of multi-compartment structure.

the highest concentration of E (20-40%), the particles formed much larger size of 650 nm to > 1 μm (Figures 4H-I). This observation was confirmed by their corresponding TEM images Figures 1H-I, which showed tiny vesicle with thick mesoporous shell and dramatically increased particle size to > 1 μm . SEM analysis for samples with co-solvents M, P, and A (Figure S3) also showed similar phenomena as observed by co-solvent E (occurrence of partition lines and particle fusion). The only difference was observed in sample 6P, which started to show the evidence of particle fusion at lower concentration compare to E, M and A. This indicates the co-solvent with longer carbon chain brought more impact on the assembly of FC vesicles compared to co-solvent with shorter carbon chain.

XRD analysis (Figure 5) showed the influence of E on the mesostructure of MCPMO samples, which gradually changed from highly ordered to less ordered structure. The XRD patterns of samples 0E, 1E, 2E, revealed three characteristic diffraction peaks at 2.42° , 4.20° , 4.80° (2θ), which could be indexed as (100), (110), and (200) symmetry and assigned as 2D hexagonal structure (space group $P6mm$). However, with the addition of 3, 6, 8, and 12 % E, their XRD patterns showed a gradual decrease of the peaks located at 2θ of 4.20° and 4.80° , which indicated the loss of long range mesostructure order. A right shift of the primary peak originally located at 2.42° , suggesting a decrease of d-spacing resulted by the interaction between HC micelles and E. Consequently the micelle self-assembly was affected and led to the variation of pore size and curvature. This influence was more obvious with the higher concentration of E, as demonstrated by wide XRD peaks of 20E and 40E samples. XRD results for samples with the addition of M, P, A

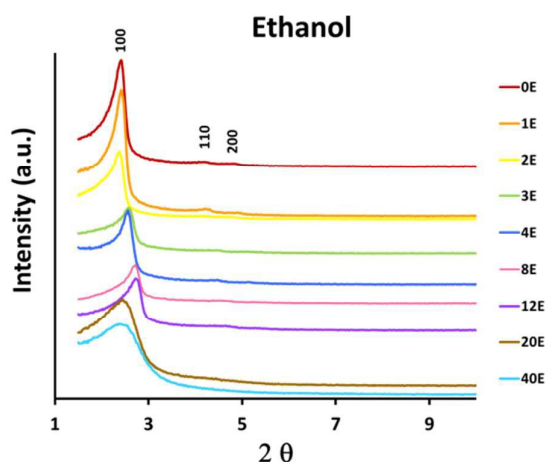


Figure 5. XRD results of MCPMO samples (0E, 1E, 2E, 3E, 6E, 8E, 12E, 20E, and 40E)

(Figure S4) showed similar trend as the addition of E, where secondary peaks located at (4–6° of 2θ) gradually disappeared by increasing concentration of the co-solvents. Interestingly, with the addition of 20% E and M the primary peaks located at 2–3° of 2θ could be maintained by 20E and 20M samples; however 20P and 20A samples already lost their primary peaks at this stage. This suggests that co-solvent P and A might diffused into the HC micelles and disrupted their pore geometries.

The nitrogen sorption isotherm results (Figure 6) showed that all E series samples possessed a small fraction of microporous region as indicated by their small uptake of nitrogen gases at low relative pressure ($P/P_0 < 0.05$). Obvious steep capillary condensation step was observed at $P/P_0 = 0.3$ for all E series samples, showing a typical mesoporous characteristic with type IV isotherm curve. A common feature of these isotherm plots is type H4 hysteresis loops in the range of $P/P_0 = 0.45$ – 0.99 , which is characteristic for sample with hollow morphologies.²⁸ Interestingly, these hysteresis loops were gradually became narrow with the increasing addition of E from 0% to 40%, which could be attributed to the gradual decrease of the vesicles size as confirmed by their TEM images Figure 1 and their physical dimension Table 1. Similar trend was also observed by the addition of co-solvents M, P and A as shown by their isotherm curves Figure S5. The BET surface area and total pore volume results of all E, M, P, and A series samples showed relatively high surface area between ~ 560 – 1100 m^2/g as well as total pore volume of 0.54 – 1.04 cm^3/g . General trends of increasing surface area were observed by increasing amount of E as shown by 2E (564.3 m^2/g) to 20E (1118.9 m^2/g). However 0E and 1E samples showed a small anomaly which might be due to the transition state from single vesicular to multi-compartment structure. Large surface area (>1000 m^2/g) and pore volume (> 0.9 cm^3/g) of samples 12E, 20E and 40E were attributed to the characteristic of tiny vesicle with thick mesoporous wall. This gradual changing of surface area and pore volume (Table 1) was contributed by the decrease of the vesicle size and their assembly behaviours as a result of the interaction between FC surfactant and E as confirmed by cryo TEM Figure 2 and TEM observation Figure 1. For samples M, P and A, there was no general trend in their surface area and total pore volume (Tables S1) as observed in E series samples.

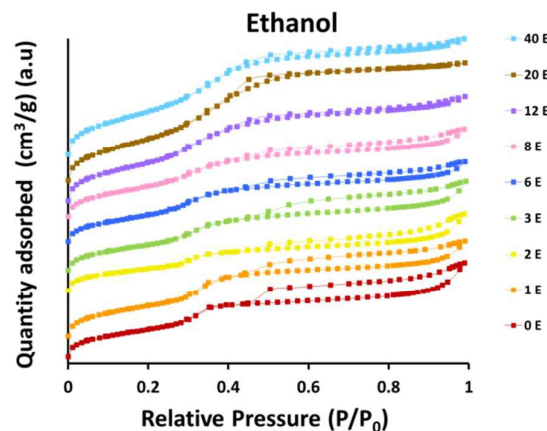
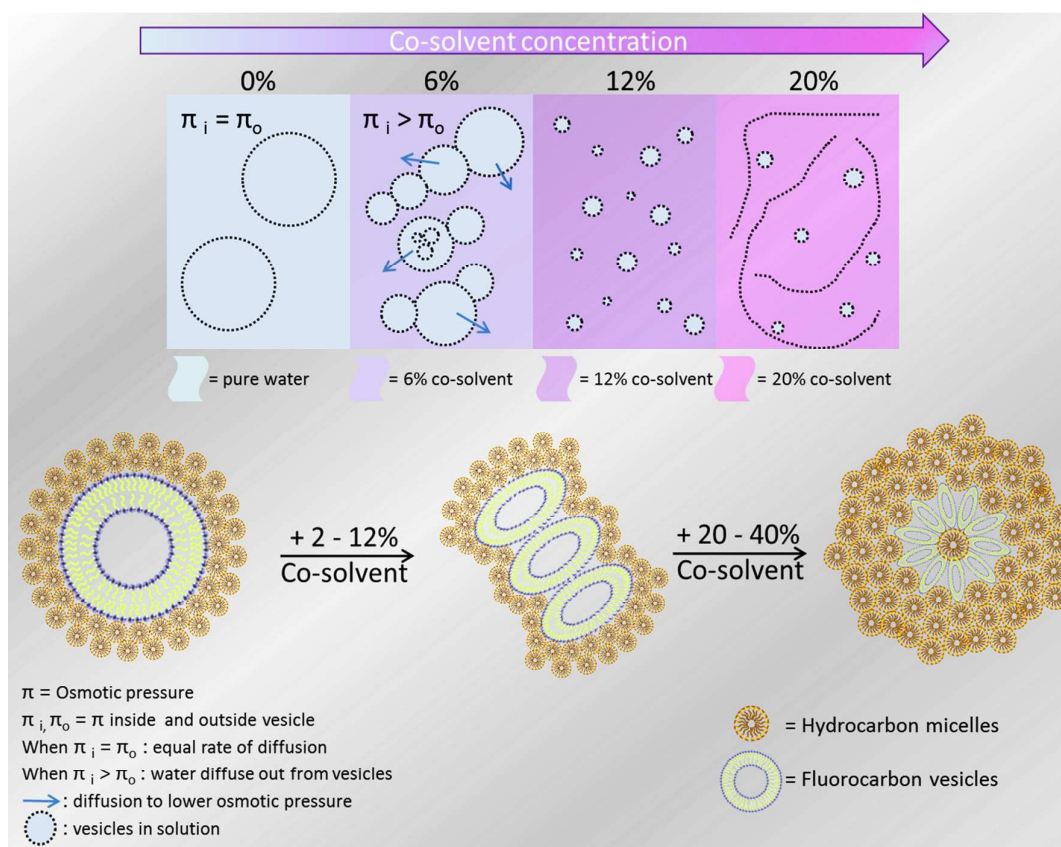


Figure 6. Nitrogen sorption isotherm curve of MCPMO samples (0E, 1E, 2E, 3E, 6E, 8E, 12E, 20E, and 40E)

Pore size distribution analysis for E series (Figure S7), M, P, and A series (Figure S6) showed that all samples possessed porosity in the mesoporous region (2–50 nm pore size). Their distribution curves (Figure S7) indicated a gradual changing from narrow pore size distribution for samples 0E, 1E and 2E (centered at 3.24 – 3.37 nm), then slightly become wider for samples 3E to 12E (centered at 3.15 – 3.25 nm) and showed bimodal peaks for samples 20E and 40E (centered at 3.4 – 3.55 nm). This changing was further confirmed by their XRD graph Figure 5, where the mesostructure was disrupted due to the increasing amount of E adsorbed into the HC micelles that affect their self-assembly behavior and lead to the less ordered structure with increasing pore size (Table 1). Similarly, Figure S6 also confirmed that higher concentration of co-solvents M, P, and A led to the gradual decrease of quality in their pore size distribution, which was in good agreement with their XRD results (Figure S4).

Formation mechanism of MCPMOs.

The formation mechanism of MCPMO samples can be explained as follow: before the addition of co-solvent E, the FC vesicles were represented as spherical bubbles with semi permeable membrane that initially contained water only. However, when E was added into the system, it created a concentration gradient that led to the osmotic pressure difference between the interior and exterior environment of the bubbles. In response to this osmotic difference, the interior water would diffuse out through the semipermeable membrane and resulted in the decrease of volume to surface ratio, triggering these bubbles to deflate into smaller size as confirmed by the TEM results (Figure 1) and their physical properties in Table 1. This osmotically driven morphological transition would trigger the outflow of aqueous solution from high to low concentration across the vesicle membrane and caused the membrane stress. When the osmotic difference reached a certain degree (E concentration $\geq 20\%$) most of the interior water content would have been diffused out, resulting in very tiny bubbles/vesicles where some of fully deflated ones were fused and transformed into thread like micelles (cryo TEM - Figure S2D). Interestingly, sample 20E (TEM - Figure 1H) showed mesoporous structure particles without obvious vesicles. However with the increasing concentration of E, some traces of small vesicles can be found from sample 40E (Figure 1I). This phenomenon might be attributed to the reversible diffusion process



Scheme 1. Schematic diagram illustrating the formation mechanism of MCPMOs

(reverse osmosis), which was triggered by the inwards osmotic pressure in the system since the liquid mixture (water and E) diffused back into those tiny vesicles and fused them into larger size of vesicles.^{32,33} The evidence of particle fusion was observed by sample 12E (TEM-Figure 1G) and this tendency became more obvious with the increasing amount of E as shown by 20E and 40E samples (SEM and TEM images Figures S4 and Figure 1). Accordingly, the vesicles fusion was also the reason for enlargement of vesicle size observed during the transition from 20E to 40E samples (Figure 1H - I). These phenomena could be referred to the similar behavior of lipid and polymeric vesicles, which undergo morphology transitions like budding, fission and fusion when they receive small changes in their environment (i.e. mixing processes, dilution, solution composition, chemical reaction, temperature, pressure, osmotic condition, and electric field).³⁴ The addition of co-solvents played a critical role in the formation of multi-compartment structure of MCPMOs, which follow the order of: 1) singular vesicles (0E); 2) vesicle fission with reduced size (1E to 8E); 3) further decrease of vesicle size (12E); 4) tiny vesicles co-exist with thread like micelles (20E); as illustrated by Scheme 1.

Drug adsorption and release study

An antimalarial and anti-tumour candidate Artemisinin (ART) was used as a model drug to investigate the potential application of MCPMOs as drug carrier in loading and release study. ART

possesses potent anti-proliferative properties that has been introduced for its anti-tumour activity through several studies including bone, lung, colon,^{35,36} breast,³⁷ cervical and HPV-related diseases,³⁸ liver,³⁹ pancreatic,⁴⁰ and prostate cancer.⁴¹ ART and its derivatives induce apoptosis in cancer cells due to iron-dependent generation of reactive oxygen species (ROS),⁴² which inhibit endothelial cell proliferation, cell migration and endothelial tube formation.⁴³ They also interfere with synthesis of vascular endothelial growth factors via suppression of hypoxia inducible factor activation.⁴⁴

In this study three samples (0E, 3E, and 6E) with different internal morphology (single vs. multi-compartment) and compartment size (225 x 225, 75 x 200, and 50 x 200 nm respectively) were used as host material. The physical properties of all samples before and after drug loading are presented in Table S2. The decreased value of pore size (21-25%); pore volume (40-54%); and surface area (22-56%) confirm the successful adsorption of the ART in all MCPMO samples. A more significant decrease of pore volume in comparison to the pore size may suggest that majority of the ART occupied the interior part of the compartments instead of the mesoporous shell of MCPMOs. The results show that MCPMOs with multi-compartment structure (3E and 6E) have considerably higher loading capacity (47 and 43.3 % respectively) compared to sample with singular compartment (0E) (35.14%). Multi-compartment feature has favored higher storage capacity by

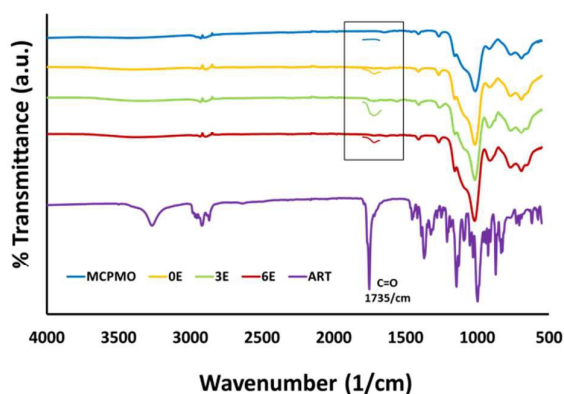


Figure 7. FTIR graph of ART loaded samples (0E, 3E and 6E), blank sample (MCPMO) and pristine ART

providing more individual-segregated spaces for drug molecules compared to the singular compartment. A slightly higher loading capacity of ART in sample 3E than 6E (4.3 % difference), could be attributed to the larger compartment size of 3E (75 x 200 nm) in contrast to 6E (50 x 200 nm) as indicated by its higher pore volume. FTIR analysis (Figure 7), further confirm the presence of ART in MCPMO samples as shown by the characteristic stretching vibration of C=O located at 1735/cm by all three ART loaded samples (0E, 3E and 6E) in contrast to unloaded sample (MCPMO). A 5x magnifications at 1735/cm wavelength region (Figure 7) clearly show the blank sample (MCPMO) has flat line indicates no ART traces exist in that sample, in contrast to the other three samples, which show the stretching vibration of C=O bond.

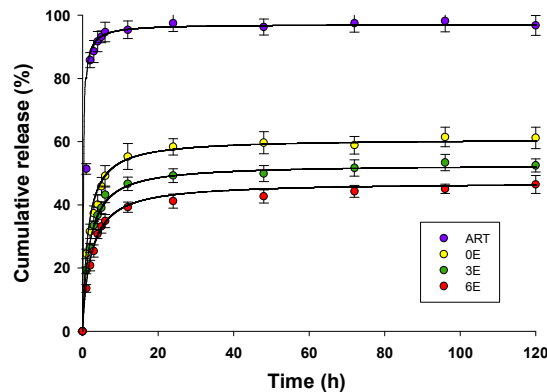
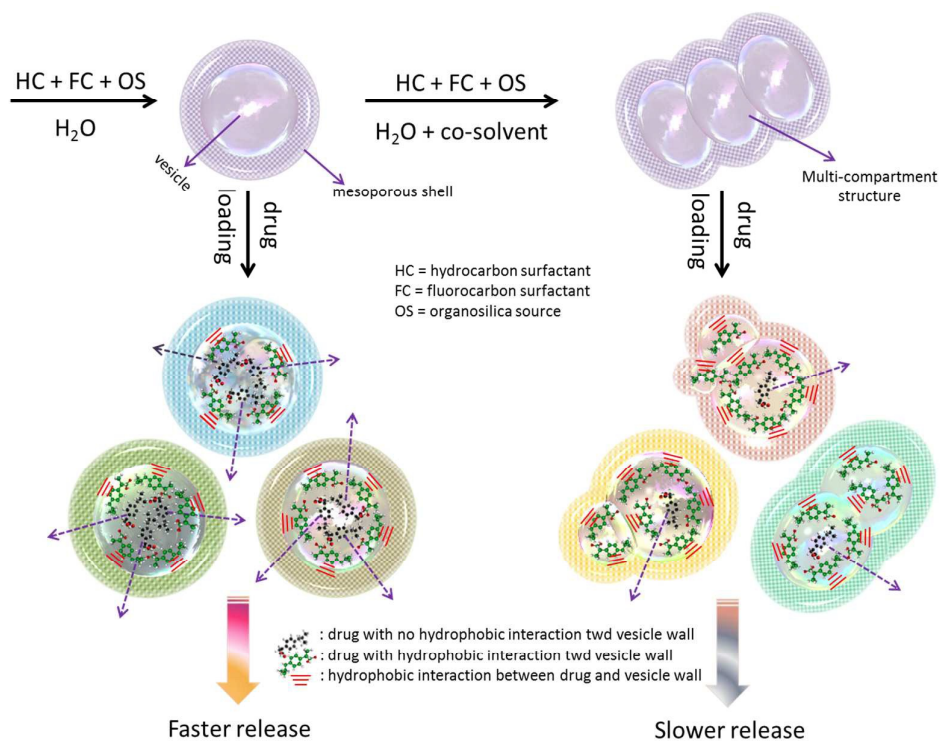


Figure 8. Cumulative release profile of pristine ART and encapsulated ART within MCPMO samples (0E, 3E, and 6E)

Drug release study was performed for the ART loaded samples (0E, 3E and 6E) also pristine ART as the reference in Phosphate Buffer solution (PBS) pH 4.4, since the endocytosis process of the major degradative system (endosomal/lysosomal) are characterised by low pH (3.8-5.0). Non-encapsulated (pristine) ART underwent rapid dissolution (>90% release) in the first 4 hr and reached equilibrium after 6hr, in contrast to the encapsulated ART. Cumulative release graph (Figure 8) showed a sustainable release profile of ART encapsulated by (0E, 3E, 6E) samples with the highest rate of the pristine ART (98%), in contrast to encapsulated ART in 0E (61.2%), followed by ART in 3E (52.5%), and ART in 6E (46.3%).



Scheme 2. Schematic diagram illustrating the hydrophobic interaction of ART molecules - host material with multi-compartment structure (right), leading to slower release compared to ART molecules encapsulated by singular compartment structure (left)

Journal Name

ARTICLE

Table 1. Physicochemical properties of MCPMO samples of MCPMO samples 0E, 1E, 2E, 3E, 6E, 8E, 12E, 20E, and 40E

Sample	BET surface area (m ² /g)	Pore volume (cm ³ /g)	Pore size (nm)	Particle size (nm) ^{SEM}	Vesicle size (nm) ^{TEM}
0E	698.3	0.82	3.24	300 - 350	225x225
1E	778.8	0.84	3.37	350 - 400	150 x200
2E	564.3	0.67	3.25	350 - 400	100 x 200
3E	699.5	0.78	3.25	300 - 400	75 x 200
6E	743.7	0.70	3.15	300 - 350	50 x 200
8E	816.6	0.77	3.16	350 - 450	40 x 150
12E	1028.8	0.92	3.17	450 - 750	30 x 130
20E	1118.9	1.04	3.55	650 - 1000	20 x 90
40E	1098.9	1.00	3.40	> 1000	10 x 100

Faster release of ART during the first 24 h might indicate the initial release of the drug molecules that occupy the mesoporous shell and followed by a slow diffusion of drug that occupy the interior region of the compartments. Within 48 hour, ART was released at ~42-50% (for 3E and 6E) and ~ 60% (for 0E). It might be contributed by the internal morphology of their host materials (single vs. multi-compartment). Interestingly, the encapsulated ART in 0E showed (~9-15%) higher release rate compared to the other two samples of (3E and 6E). An increasing number of compartments inside each particle may provide more surface contact between drug molecules and the vesicle wall of the host materials. The hydrophobic features of MCPMOs framework might offer better affinity between hydrophobic drug molecules and their compartment walls. This could lead to a slower diffusion of ART from the host material with multi-compartment structure (3E and 6E) in contrast to the single compartment sample (0E) as illustrated in Scheme 2.

Drug release kinetic study

In order to get better understanding on the quantitative information of the drug dissolution process, a mathematical model was developed. The curve fitting of mass transfer model for the experimental data of drug release are depicted as solid lines in Figure 8. This empirical approach is employed to predict the release profile of ART in PBS medium, which showed pseudo second order mechanism described as follows:

$$\frac{dC_A}{dt} = k(C_{Ac} - C_A)^2 \quad (1)$$

where C_A and C_{Ac} are concentration of drug in the bulk liquid at time t and at equilibrium, respectively, k is second-order constant. Integrating equation (1) with boundary conditions of at the beginning ($t = 0$), $C_A = 0$, and at time t , $C_A = C_A$ to obtain

$$C_A = \frac{C_{Ac}^2 k t}{(1 + C_{Ac} k t)} \quad (2)$$

Re-writing Equation (2) in term of equilibrium percentage release, R_e , gives

$$R = \frac{R_e^2 k t}{\left(\frac{1}{C_o} + R_e k t\right)} \quad (3)$$

where C_o is initial drug loading in (mg/L), and R is the percentage of drug release in the solution. Both of these parameters are obtained by non-linear regression method that fit the experimental data.

Conclusions

We have introduced a facile synthesis route in preparing MCPMOs with complex morphology through synergetic interaction between hydrocarbon (HC) - fluorocarbon (FC) surfactants and organosilane in the presence of co-solvents, which induce the formation of multi-compartment structure. The isolated compartments in MCPMOs can offer potential advantage for selective encapsulation of various active agents and prevent any undesired interactions before reaching the target. Their drug adsorption and release study demonstrate higher adsorption capacity (up to 47%) and slower release rate (46% in 120 hr) compared to conventional mesoporous silica and organosilica materials due to their unique multi-compartment structure and hydrophobic properties. This approach may provide a simple strategy to generate bio-inspired nanomaterials that mimic the properties and function of eukaryotic cell to benefit various applications in medical treatment, catalysis, energy storage and environmental field.

Acknowledgements

C.X. Lin is grateful to Prof. Cheng Zhong Yu, Prof. Max Lu, Dr Lei Zhang, Dr Jie Yang, Dr Garry Morgan and Dr Zhi Gang Xiong for discussion and help. The authors acknowledge the facilities of the ARC Centre of Excellence for Functional Nanomaterials,

Australian Microscopy & Microanalysis Research Facility at the Centre for Microscopy & Microanalysis, The University of Queensland. The Australian Research Council is acknowledged for funding project FT100100879. CHZ acknowledge the financial support from the NNSFC 21373185.

References

- 1 J. Du, J. and R.K. O'Reilly, *Chemical Society Reviews* 2011, **40**, 2402.
- 2 S. Mitragotri and J. Lahann, *Nature Materials* 2009, **8**, 15.
- 3 C.E. Ashley, E.C. Carnes, G.K. Phillips, D. Padilla, P.N. Durfee, P.A. Brown, T.N. Hanna, J. Liu, B. Phillips, M.B. Carter, N.J. Carroll, X. Jiang, D.R. Dunphy, C.L. Willman, D.N. Petsev, D.G. Evans, A.N. Parikh, B. Chackerian, W. Wharton, D.S. Peabody and C.J. Brinker, *Nature Materials* 2011, **10**, 389.
- 4 Z.B. Li, E. Kesselman, Y. Talmon, M.A. Hillmyer and T.P. Lodge, *Science* 2004, **306**, 98.
- 5 A.H. Groeschel, F.H. Schacher, H. Schmalz, O.V. Borisov, E.B. Zhulina, A. Walther and A.H.E. Mueller, *Nature Communications* 2012, **3**, 710.
- 6 J. Zhu, S. Zhang, F. Zhang, K.L. Wooley and D.J. Pochan, *Advanced Functional Materials* 2013, **23**, 1767.
- 7 C. Boyer and J.A. Zasadzinski, *ACS Nano* 2007, **1**, 176.
- 8 S. Bhaskar, J. Hitt, S.W. Chang and J. Lahann, *Angewandte Chemie-International Edition* 2009, **48**, 4589.
- 9 K.J. Lee, J. Yoon, S. Rahmani, S. Hwang, S. Bhaskar, S. Mitragotri and J. Lahann, *Proceedings of the National Academy of Sciences of the United States of America* 2012, **109**, 16057.
- 10 V.P. Torchilin, *Nature Reviews Drug Discovery* 2005, **4**, 145.
- 11 M. Yokoyama, *Journal of Drug Targeting* 2014, **22**, 576.
- 12 M. Benezra, O. Penate-Medina, P. B. Zanzonico, D. Schaer, H. Ow, A. Burns, E. DeStanchina, V. Longo, E. Herz, S. Iyer, J. Wolchok, S.M. Larson, U. Wiesner and M.S. Bradbury, *Journal of Clinical Investigation* 2011, **121**, 2768.
- 13 T. Asefa, M. J. MacLachlan, N. Coombs and G. A. Ozin, *Nature* 1999, **402**, 867.
- 14 S. Inagaki, S. Guan, Y. Fukushima, T. Ohsuna and O. Terasaki, *Journal of the American Chemical Society* 1999, **121**, 9611.
- 15 B.J. Melde, B.T. Holland, C. F. Blanford and A. Stein, *Chemistry of Materials* 1999, **11**, 3302.
- 16 S.S. Park, M. S. Moorthy and C.S. Ha, *NPG Asia Materials* 2014, **6**.
- 17 N. Mizoshita, T. Tani and S. Inagaki, *Chemical Society Reviews* 2011, **40**, 789.
- 18 C.X. Lin, S. Z. Qiao, C.Z. Yu, S. Ismadji and G.Q. Lu, *Microporous and Mesoporous Materials* 2009, **117**, 213.
- 19 C.X.C. Lin, Z. Li, S. Brumbley, L. Petrasovits, R. McQualter, C. Yu, G. Q. (Max) Lu, *Journal of Materials Chemistry*, 2011, **21**, 7565.
- 20 C. Urata, H. Yamada, R. Wakabayashi, Y. Aoyama, S. Hirotsawa, S. Arai, S. Takeoka, Y. Yamauchi and K. Kuroda, *Journal of the American Chemical Society* 2011, **133**, 8102.
- 21 J. Croissant, X. Cattoen, M.W.C. Man, A. Gallud, L. Raehm, P. Trens, M. Maynadier and J.O. Durand, *Advanced Materials* 2014, **26**, 6174.
- 22 P. Van der Voort, D. Esquivel, E. De Canck, F. Goethals, I. Van Driessche and F.J. Romero-Salguero, *Chemical Society Reviews* 2013, **42**, 3913.
- 23 S.Z. Qiao, C. X. Lin, Y.G. Jin, Z. Li, Z.P. Hao, Z.M. Yan, Y.N. Huang, G. Q. Lu, *Journal of Physical Chemistry C*, 2009, **113**, 8673.
- 24 C. Sanchez, P. Belleville, M. Popall and L. Nicole, *Chemical Society Reviews* 2011, **40**, 696.
- 25 H. Cui, Z. Chen, S. Zhong, K.L. Wooley and D.J. Pochan, *Science* 2007, **317**, 647.
- 26 S. Kubowicz, A. F. Thunemann, R. Weberskirch and H. Mohwald, *Langmuir* 2005, **21**, 7214.
- 27 A.O. Moughton, M.A. Hillmyer and T.P. Lodge, *Macromolecules* 2012, **45**, 2.
- 28 C.X. Lin, P. Yuan, C.Z. Yu, S.Z. Qiao and G.Q. Lu, *Microporous and Mesoporous Materials* 2009, **126**, 253.
- 29 M.P. Krafft and J.G. Riess, *Chemical Reviews* 2009, **109**, 1714.
- 30 R. Lipowsky, M. Brinkmann, R. Dimova, T. Franke, J. Kierfeld and X.Z. Zhang, *Journal of Physics-Condensed Matter* 2005, **17**, S537.
- 31 H. Djojoputro, X.F. Zhou, S.Z. Qiao, L.Z. Wang, C.Z. Yu and G.Q. Lu, *Journal of the American Chemical Society* 2006, **128**, 6320.
- 32 A.J. Markvoort, P. Spijker, A.F. Smeijers, K. Pieterse, R.A. van Santen and P.A.J. Hilbers, *Journal of Physical Chemistry B* 2009, **113**, 8731.
- 33 S. Segota and D. Tezak, *Advances in Colloid and Interface Science* 2006, **121**, 51.
- 34 R. Dimova and R. Lipowsky, *Soft Matter* 2012, **8**, 6409.
- 35 D.M. Rubush, M.A. Morges, B.J. Rose, D.H. Thamm and T. Rovis, *Journal of the American Chemical Society* 2012, **134**, 13554.
- 36 W.M. Liu, A. M. Gravett and A. G. Dalgleish, *International Journal of Cancer* 2011, **128**, 1471.
- 37 A.S. Tin, S. N. Sundar, K.Q. Tran, A.H. Park, K.M. Poindexter and G.L. Firestone, *Anti-Cancer Drugs* 2012, **23**, 370.
- 38 S.K. Goodrich, C.R. Schlegel, G. Wang and J.L. Belinson, *Future Oncology* 2014, **10**, 647.
- 39 J. Hou, D. Wang, R. Zhang and H. Wang, *Clinical Cancer Research* 2008, **14**, 5519.
- 40 S.J. Wang, Y. Gao, H. Chen, R. Kong, H.C. Jiang, S.H. Pan, D. B. Xue, X.W. Bai and B. Sun, *Cancer Letters* 2010, **293**, 99.
- 41 I. Nakase, B. Gallis, T. Takatani-Nakase, S. Oh, E. Lacoste, N.P. Singh, D. R. Goodlett, S. Tanaka, S. Futaki, H. Lai and T. Sasaki, *Cancer Letters* 2009, **274**, 290.
- 42 I. Nakase, H. Lai, N.P. Singh and T. Sasaki, *International Journal of Pharmaceutics* 2008, **354**, 28.
- 43 H.H. Chen, H.J. Zhou, G.D. Wu and X.E. Lou, *Pharmacology* 2004, **71**, 1.
- 44 X.J. Huang, Z.Q. Ma, W.P. Zhang, Y.B. Lu and E.Q. Wei, *Journal of Pharmacy and Pharmacology* 2007, **59**, 849.